Modeling and Estimation Problems in the Turtle Visual Cortex

Zoran Nenadic*, Bijoy K. Ghosh, *Fellow, IEEE*, and Philip S. Ulinski

Abstract—The goal of this paper is to verify that position and velocity of a spot of light incident on the retina of a turtle are encoded by the spatiotemporal dynamics of the cortical waves they generate. This conjecture is examined using a biophysically realistic large-scale computational model of the visual cortex implemented with the software package, GENESIS. The cortical waves are recorded and analyzed using principal components analysis and the position and velocity information from visual space is mapped onto an abstract B-space, to be described, using the coefficients of the principal components expansion. The likely values of the position/velocity are estimated using standard statistical detection methods.

Index Terms—Cortical wave, detection, principal components, visual cortex.

I. INTRODUCTION AND DESCRIPTION OF THE TURTLE VISUAL CORTEX

MAMMALS have a cerebral cortex that embodies several, topographically organized representations of visual space. Extracellular recordings show that neurons in a restricted region of visual cortex are activated when a visual stimulus is presented to a restricted region of the visual space, the classical receptive field of the neuron [1]. Neurons at adjacent points in the cortex are activated by stimuli presented at adjacent regions of the visual space. Consequently, there is a continuous but deformed map of the coordinates of visual space to the co-ordinates of the cortex. Extracellular recordings from the visual cortex of freshwater turtles produced a different result [2]. Neurons at each cortical locus are activated by visual stimuli presented at every point in the binocular visual space, although the latency and shape of the response waveforms vary as the stimulus is presented at different loci in the visual space. This suggests that there may not be a simple map of the coordinates of the visual space to the coordinates of the visual cortex in turtles. Position in the visual space is either not represented in the visual cortex, or is represented in some form other than a retinotopic map. Experiments conducted by Senseman [3] and Senseman and Robbins [4], [5] have supported this viewpoint.

*Z. Nenadic was with the Department of Systems Science and Mathematics, Washington University, St. Louis, MO 63130 USA. He is now with the Division of Engineering and Applied Science, California Institute of Technology, Mail Stop 104–44, Pasadena, CA 91125 USA (e-mail: zoran@caltech.edu).

B. K. Ghosh is with the Department of Systems Science and Mathematics, Washington University, St. Louis, MO 63130 USA.

P. S. Ulinski is with the Department of Organizmal Biology and Anatomy, University of Chicago, Chicago, IL 60637 USA.

They used voltage-sensitive dye methods to show that presentation of a visual stimulus to the retina of an *in vitro* preparation of the turtle eye and brain produces a wave of depolarization that propagates anisotropically across the cortex. They used a principal components method, the Karhunen–Loeve (KL) decomposition, to analyze the wave data. Individual waves could be represented as a weighted sum of as few as three eigenvectors which are functions of the coordinates of the cortex. Interestingly, presentation of different visual stimuli, such as spots of light at different points in the visual space, produce waves that have different representations in the three dimensional (3-D) eigenspace. This raises the possibility that visual information is coded in the spatiotemporal dynamics of the cortical waves. Subsequent research work provided abundant evidence that the traveling electrical waves were observed not only in turtle visual cortex [6], but also across olfactory, visual, and visuomotor areas of cortex in a variety of species [7].

The turtle visual cortex contains at least 11 morphologically distinct types of neurons, only some of which are well characterized. These are two subtypes of pyramidal cells, the lateral and medial pyramidal cells, stellate cells, and horizontal cells. Pyramidal cells have somata located in the intermediate layer 2 of the cortex and are predominantly excitatory. Stellate cells have somata in the outer layer 1 and are inhibitory. Horizontal cells have somata in layer 3 and are also inhibitory. Pyramidal cells and stellate cells receive direct projections from the dorsal lateral geniculate complex (LGN) [8]. Geniculate axons intersect lateral and medial pyramidal cells in characteristic patterns that will be described later [9]. These synapses have experimentally been determined as the α-amino-3 hydroxy-5 methyl-4 isoxazole proprionic acid (AMPA) subtype of glutamate receptor [10]. Pyramidal cells make projections to stellate cells, horizontal cells and other pyramidal cells. Their synapses access both AMPA and N-methyl-D-aspartate receptors [10]. Likewise, stellate cells and horizontal cells make feedback projections to pyramidal cells. These synapses access both $GABA_A$ and $GABA_B$ receptors. Finally, stellate cells project back to stellate cells via synapses that access $GABA_A$ and $GABA_B$ receptors [11].

We constructed a large-scale model of the turtle visual cortex that has the ability to simulate cortical waves with the same qualitative features as the cortical waves seen in experimental preparations. After the model had been constructed, the wave data were analyzed using principal components analysis (PCA). This leads to a convenient representation of a large-dimensional data set in a low-dimensional subspace. The responses of the model to a localized stationary stimulus and a stimulus moving with constant velocity have been studied in particular. Finally, we
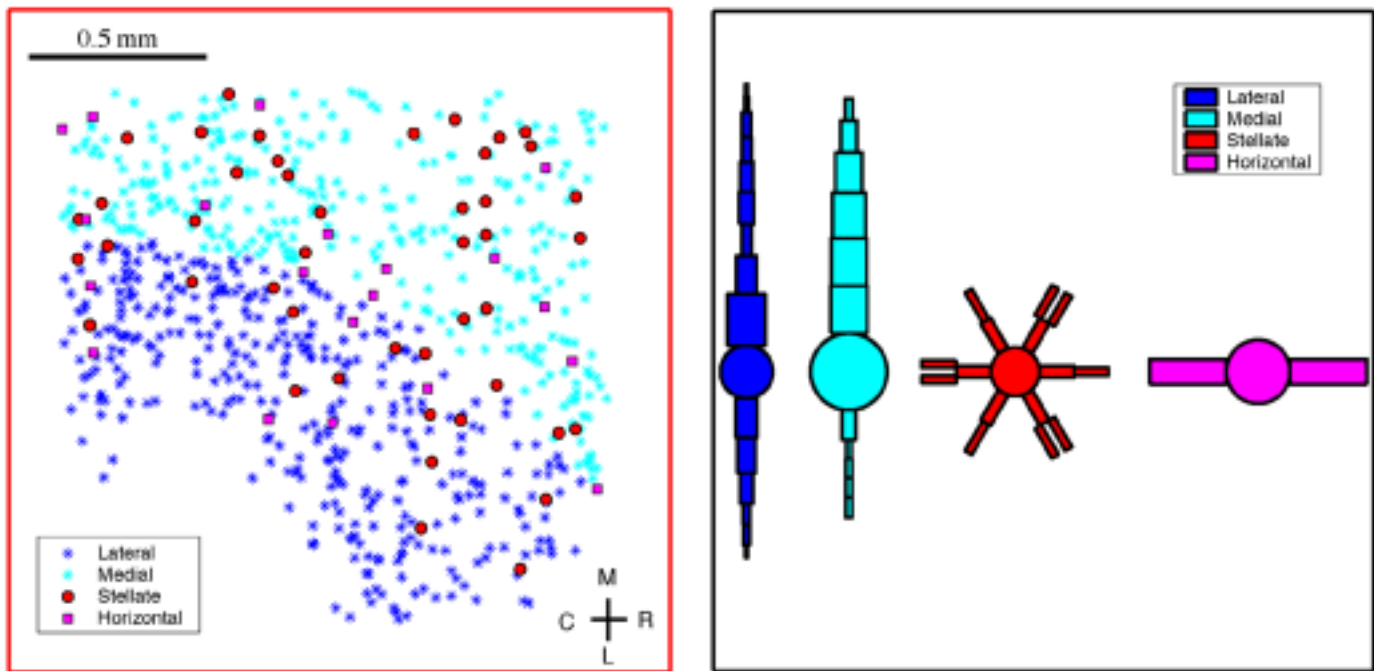
Fig. 1. (left) Three layers of turtle visual cortex projected onto a single plane. Different colors indicate different cell types. The total number of cortical cells is 750 and the relative densities of cells are preserved with respect to experimental data. The crossbar indicates the position of rostral (R), caudal (C), lateral (L), and medial (M) part of the cortex. (right) Compartmental structure of lateral, medial, stellate, and horizontal cells. The spherical compartments represent somata and the cylindrical compartments are parts of dendrites. Axons are modeled as delays and are not shown in the figure.

use standard statistical methods [Bayesian and maximum-likelihood (ML)] to estimate the parameters of unknown stimuli, based on the cortical response they elicit. The results suggest that the cortical wave indeed carries information about the position and velocity of the stimulus. However, an important caveat is that we do not yet know if the turtle uses this information in the cortical wave.

II. DESCRIPTION OF THE MODEL

In this section, we will give a brief description of the large-scale model of turtle visual cortex. Modeling, in general, is an evolutionary process and involves numerous parameters, some of which are obtained by physiological measurements and some of which are simply tuned in the modeling process. Comprehensive description of the computational model goes beyond the scope of this paper and can be found in [12]. Briefly, the dimensions of the somata and dendrites of individual types of neurons were based on measurements from Golgi impregnations of turtle visual cortex [13]. Biophysical parameters for each cell type were measured with *in vivo* intracellular recording methods [14], [15]. The physiology of each type of synapse included in the model is known from *in vitro* intracellular recording experiments [10]. The kinetics of individual types of voltage-gated channels have not been characterized with voltage-clamp methods in turtle visual cortex, so the parameters needed to implement Hodgkin–Huxley-like kinetic schemes were obtained from work on mammalian cortex and constrained by comparing the firing patterns of model cells to real cells following intracellular current injections. The geometry of the geniculocortical and intracortical interconnections

are known in detail [9], [16]. There is some information on the basic shape and dimensions of the axonal arbors of stellate and horizontal cells from Golgi preparations. This data was used to estimate spheres of influence between stellate and horizontal cells and their postsynaptic targets.

The visual cortex of freshwater turtles contains three layers. The intermediate layer 2 contains principally pyramidal cells with dendrites that extend into layers 1 and 3. The outer layer 1 and inner layer 3 contain mainly inhibitory interneurons. Geniculate afferents make excitatory synapses upon the dendrites and somata of pyramidal cells and the dendrites and somata of layer 1 neurons. Our model assumes the three layers are projected onto a single plane (see Fig. 1). Each neuron is represented by a multi compartmental model based on the anatomy of pyramidal neurons and inhibitory interneurons. Each compartment is modeled by a standard membrane equation and implemented in GENESIS [17]. The somata are modeled as spherical compartments and the dendrites are modeled as cylindrical compartments. The axons are not modeled as compartments but as delay lines. For a detailed description of compartmental models see [18]. In Fig. 1, we show the compartmental structure of cortical interneurons. Maps of the spatial distribution of neurons in each of the three layers of the cortex were constructed from coronal sections through visual cortex of a turtle. The maps were divided into an 8×56 array of rectangular areas, each measuring 28×190 μm. Experimental data were not available for each of the 8×56 rectangular boxes and were interpolated at locations where measurements were not available. An algorithm was developed in MATLAB that constructed an array of neurons in each layer that preserved the ratios of cells between layers in the real cortex. The cells are distributed between 8×56 blocks according to the actual density information. Within each block,
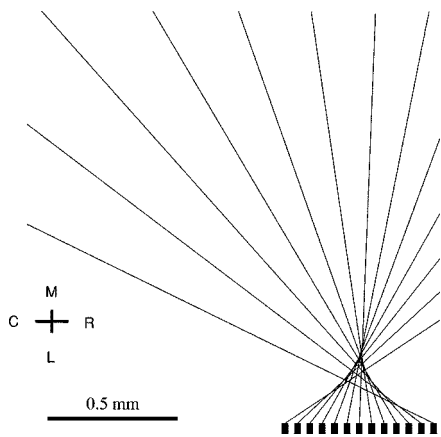
Fig. 2. Linear arrangement of geniculate neurons. The somata are shown as boxes and the corresponding axons are shown as lines. Only 13 out of 801 LGN neurons are shown for clarity.
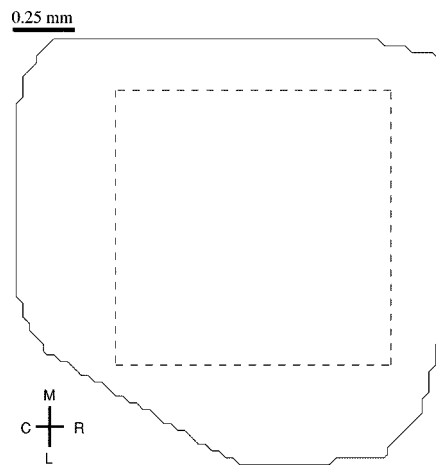

Fig. 4. Convex hull of polygon of cell coordinates. Only pixels lying inside this contour will be assigned a real value, based on triangular interpolation. Dashed lines describe the boundaries of the subimages.
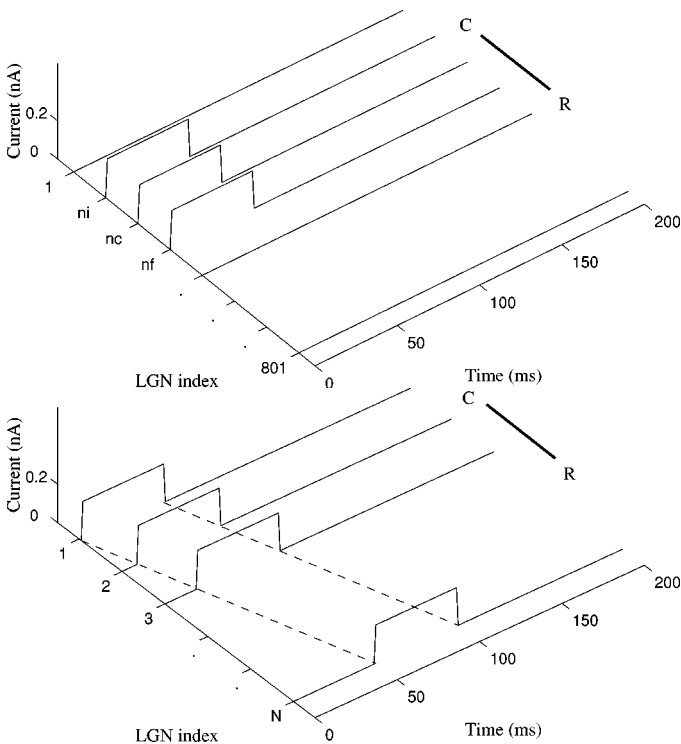

Fig. 3. (top) Simulation of a localized stationary stimulus. A group of LGN neurons indexed from n_i (initial), via n_c (central), to n_f (final) is simultaneously stimulated by a square current pulse with duration of 50 ms and amplitude of 0.2 nA. The family of stationary stimuli is parameterized by the location of the center n_c of the stimulus. (bottom) Simulation of a stimulus moving with a constant velocity. LGN neurons are sequentially stimulated by a square current pulse with duration of 50 ms and amplitude of 0.2 nA. The family of moving stimuli is parameterized by the delay of one square pulse with respect to its neighbor (slope of the dashed line).

the cell coordinates are chosen randomly from a uniform distribution, independently for every block. This algorithm is convenient as it can generate as many different models as needed, while retaining the information about the relative densities of cells in the visual cortex of a real turtle. Most of our models have approximately 680 pyramidal cells, 50 stellate cells, and 20 horizontal cells (Fig. 1). Due to the nature of the distribution

algorithm, the total number of neurons can not be guaranteed *a priori*. However, the proposed model contains nominally 750 neurons with the actual numbers varying slightly from simulation to simulation. Biophysical data are not available for neurons in the dorsal LGN of turtles, so geniculate neurons were modeled as single isopotential compartments with a spike generating mechanism. Geniculate axons are modeled as delay lines that extend across the cortex from lateral to medial. The number of geniculate neurons in the model is $L = 801$. The LGN neurons are linearly arranged along the lateral edge of the cortex with axons extending to the cortex (Fig. 2). The axons of the most rostral and most caudal LGN neurons in the array extend to the caudal and rostral poles of the cortex, respectively. The other afferents are evenly spaced between these two axons. Geniculate afferents enter the cortex at its lateral edge, cross over each other and then run in relatively straight lines from lateral to medial cortex. The rostrocaudal axis of the geniculate is consequently mapped along the caudorostral axis of the cortex. The geometry of the geniculate afferents and their spatial distribution are based on anatomical data from [9]. The number of synaptic sites (varicosities) assigned to each geniculate afferent is calculated by multiplying the length of the axon by the average number of varicosities per 100 μm of axon length. The spatial positions of the individual varicosities (the total of approximately 11 300 varicosities has been used) are assigned to axons using the distribution of varicosities along the lengths of real axons [9]. The distribution is strongly skewed to the left, indicating a greater number of varicosities in the lateral than in the medial part of the visual cortex. For cortico–cortical connections, we constructed spheres of influence. Therefore, a cortical neuron will be connected to any other cell in the cortex within its sphere of influence. The synaptic strengths were higher in the center of influence and were linearly reduced with the distance. Propagation times between neurons are calculated using the distance between a pair of neurons and conduction velocities. The conduction velocity for geniculate afferents in turtle visual cortex has been measured at 0.18 m/s [13]. Cortico–cortical connections are given conduction velocities of 0.05 m/s, consistent with measurements of propagating waves in the turtle visual cortex
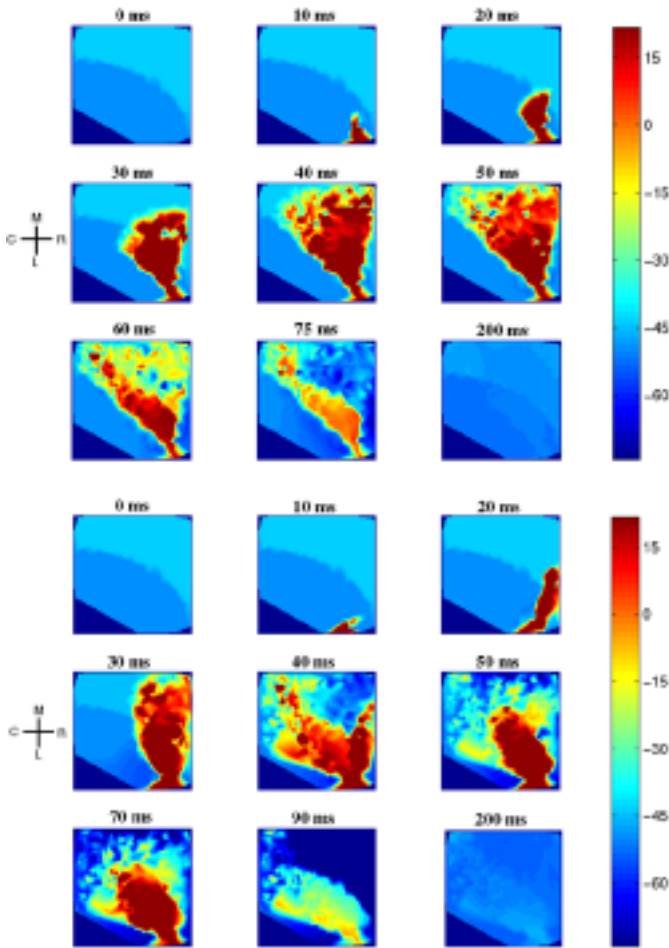
Fig. 5. Selected snapshots from the movies corresponding to different stimuli. Time is measured with respect to the onset of a stimulus, and the membrane potentials of individual cells (pixels) are color coded (the values near the color bars are in millivolts). Lateral and medial pyramidal cells have different values of resting membrane potentials, hence the difference in color at time 0 ms. The borders of darker color in each snapshot indicate that these pixels lie outside the convex hull of the polygon of cell coordinates. (top) Snapshots from the movie corresponding to one of the inputs from the family of stationary localized stimuli. (bottom) Snapshots from the movie corresponding to one of the inputs from the family of moving stimuli.

[3], and the conduction velocities for axons of inhibitory interneurons in rat cortex [19].

III. SIMULATION OF STATIONARY AND MOVING STIMULI

The stationary stimulus has been simulated by presenting a 50 ms square current pulse to a set of adjacent geniculate neurons (see Fig. 3). For the purpose of our simulation, 20 equidistant positions of the stimuli have been chosen across the LGN. The stimuli are labeled from 1 to 20, each input being parameterized by the position of the center of the square pulse n_c with respect to the LGN neurons. Therefore, *input 1* (most caudal input) corresponds to a square pulse centered at the LGN neuron 201 ($n_c = 201$), and *input 20* (most rostral input) corresponds to a square pulse centered at the LGN neuron 601 ($n_c = 601$). The other inputs are linearly distributed between the two extrema. The moving stimulus is assumed to be sweeping across the geniculate complex, from caudal to rostral, and it consists of a sequence of square pulses, equal in amplitude and duration,
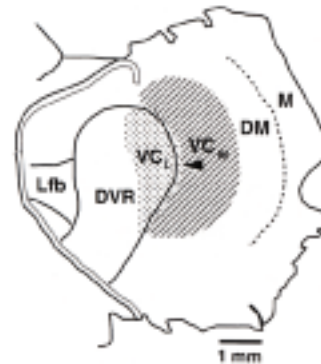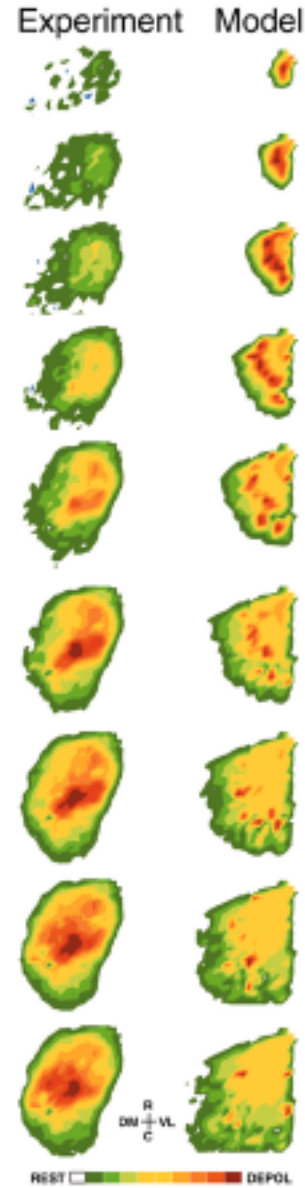

Fig. 6. (top) Comparison of wave propagation of experimental and model data. Both waves are induced by localized stationary stimuli, presenting a spot of light in experimental setup and injecting localized square current pulses in the model. The activities of individual neurons are color coded, as indicated by the color bar at bottom. (bottom) Location and nomenclature of cortical structures referenced in this paper: lateral visual cortex (VC_L), medial visual cortex (VC_M), and dorsomedial cortex (DM). Figure courtesy of David M. Senseman.

which have been delayed with respect to each other (see Fig. 3). The delay is varied linearly between two preselected values. A

set of 18 equally spaced delay parameters has been chosen between the above maximum and minimum values. The velocity of the slowest signal is therefore calculated at 0.006 m/s (*input 20*), and the velocity of the fastest signal is 0.03 m/s (*input 1*), where these values do not represent the velocities of moving stimuli in visual space but in the space of LGN. The other inputs are linearly distributed between the fastest and slowest. The overall simulation time is set to 200 ms, as we would like to observe the behavior of the system in the steady state. While this calibration in the local LGN coordinate system is useful and makes simulations easily tractable, it should not be in any way associated with the position and velocity in the visual space, as the model has not been calibrated to units of visual arc.

Since the exact locations of individual cells are randomized, we generated 50 different cortical networks using the algorithm described earlier. By running 20 stimuli on 50 different networks with the same initial conditions, we have obtained a set of 1000 simulations for both stationary and moving stimuli. The simulation results consisting of membrane potentials of individual neurons have been recorded and saved in a data file. Even though the data for all neurons are available, we are primarily concerned with the pyramidal neurons. The responses of pyramidal neurons have been visualized as movies. The data have been spatially resampled from a nonuniform grid of neuron coordinates to an artificially constructed $n \times n$ uniform grid. The program uses triangle-based linear interpolation, although other methods are also available (triangle-based cubic interpolation, nearest neighbor interpolation, etc.). The choice of interpolation algorithm did not affect the results. Triangle-based algorithm constructs a triangular grid of scattered data points (cell coordinates), and assign a value to pixels that are in interior of the triangles. The out of range data cannot be assigned any real number value and those pixels are assigned NaN.[1] In other words, the algorithm cannot extrapolate and the pixels lying outside the convex hull of polygon of cell coordinates are all assigned the value of NaN. The convex hull of the polygon of cell coordinates for one of 50 cortical samples is shown in Fig. 4. The value of membrane potential at each pixel was color coded and the spikes were not removed in the process. Selected snapshots from movies corresponding to both stationary and moving stimuli are shown in Fig. 5. The comparison of experimental and model waves is shown in Fig. 6. The purpose of this figure is to show that two waves have similar features, they originate from the same point in the cortex (rostrolateral edge) and they propagate in both rostrocaudal and mediolateral directions. It should be noted however, that the regions of the cortex observed by experiment and model are not quite identical. Senseman [20] records from dorsomedial cortex (DM) and the medial part of the visual cortex (VC$_M$), whereas our model is confined to the medial and lateral parts of the visual cortex, (VC$_M$) and (VC$_L$) respectively. Furthermore, the nature of the signals represented by Fig. 6 is different for experimental and model generated data. Experiments use voltage-sensitive dye signals, which are proportional to the membrane potentials of individual neurons and do not completely resolve individual action potentials. The model generates membrane potentials which include action potentials. Finally, the stimuli in the experimental setup are (localized) retinal light flashes where the stimuli in the model are injected square current pulses.

Let $I(x, y, t)$ denote the spatiotemporal signal of response of the model to different stimuli. Then $I(x, y, t)$ can be viewed as a collection of movie frames (snapshots). Given that every frame is $n \times n$ pixels, and every movie has m frames, it is clear that the dimension of $I(x, y, t)$ could be very high ($n \times n \times m$). Furthermore, a comparison of two different responses (movies) is of interest, as we would like to quantify the differences and similarities between them. Therefore, an efficient way for movie comparison has to be found. We now proceed to describe a principal-components-based technique for such a comparison. This method was also used earlier by Senseman and Robbins for the analysis of the data recorded from the cortex of a real turtle [4], [5].

PCA was introduced independently by many authors at different times. The method is widely used in various disciplines such as image and signal processing, data compression, fluid dynamics, partial differential equations, weather prediction, etc. [21]. In image processing, the method is used for removing a redundancy (decorrelating pixels) from images [22]. The transformation itself is linear, and represents a rotation of a coordinate system, so that neighboring pixels in the new coordinate system are less correlated. Moreover, the rotation proposed by the method is optimal as it leads to a complete removal of the correlation from neighboring pixels, which is equivalent to diagonalizing the image correlation matrix. Consequently, the image can be approximated in a low-dimensional subspace, using only selected basis vectors, also called principal eigenvectors. In the theory of partial differential equations, the method is useful for finding a separable approximation to the solution of a partial differential equation, which is optimal in the sense that it maximizes the kinetic energy cost functional [23]. Depending on the context, the method goes by the names: KL decomposition, proper orthogonal decomposition, Hotelling decomposition and singular value decomposition. We shall refer to it as KL decomposition. In the KL decomposition, an $n \times n$ pixel frame is written as a vector, u_i, of size $n^2 \times 1$. Therefore, the kth spatiotemporal signal can be viewed as a collection of frames

$$I^k(x, y, t) = \{u_1^k, u_2^k, \ldots, u_m^k\}$$

where m is the total number of frames (time samples). The average correlation matrix $C_1 \in \mathbb{R}^{n^2 \times n^2}$ for a family of N movies is then calculated as

$$C_1 = \frac{1}{Nm} \sum_{k=1}^{N} \sum_{i=1}^{m} (u_i^k)(u_i^k)^T. \tag{1}$$

The matrix C_1 is symmetric and positive semidefinite, so its eigenvalues are all real and nonnegative and the corresponding eigenvectors are orthonormal and form a basis in $\mathbb{R}^{n^2}$. This basis will be referred to as *global basis*. The eigenvectors corresponding to the largest p eigenvalues of C_1 are called the principal eigenvectors (modes) and the pth-order successive reconstruction of the spatiotemporal signal $I^k(x, y, t)$ is given by

$$\hat{I}^k(x, y, t) = \sum_{i=1}^{p} \alpha_i^k(t) M_i(x, y) \tag{2}$$

where $M_i(x, y) \in \mathbb{R}^{n^2 \times 1}$ are the principal modes, the time coefficients $\alpha_i(t)$ are given by $\alpha_i^k(t) = \langle I^k(x, y, t), M_i(x, y) \rangle$,

---

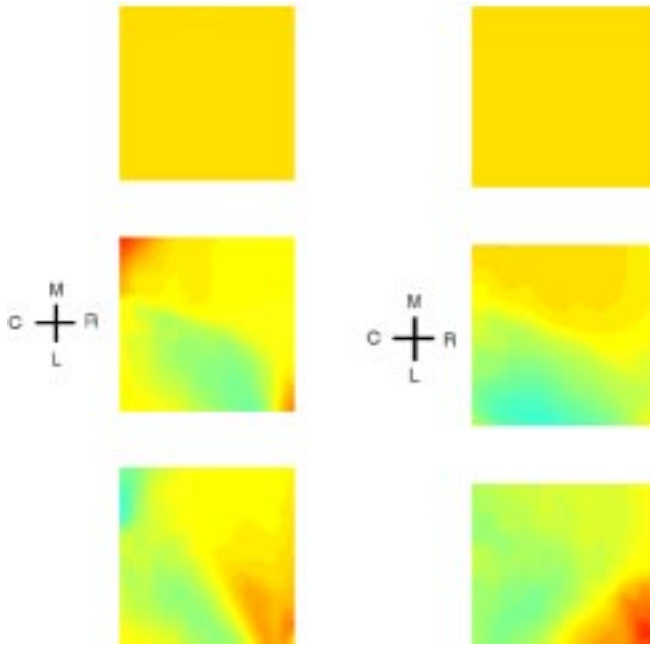[1]The IEEE arithmetic representation for not-a-number (NaN).

Fig. 7. (left) Three spatial principal modes corresponding to stationary data global basis. Modes are displayed as images: (top) $M_1(x, y)$, (middle) $M_2(x, y)$, and (bottom) $M_3(x, y)$. (right) Equivalent picture for moving data global basis. Both bases are calculated based on 1000 movies.

Fig. 9. (top) Presentation of a localized stationary stimulus at different positions (three for experiment and five for model) in the visual space. (middle) Corresponding phase trajectories in A-space. (bottom) Clusters of points in B-space as a result of repeated trials. Figure courtesy of David M. Senseman.
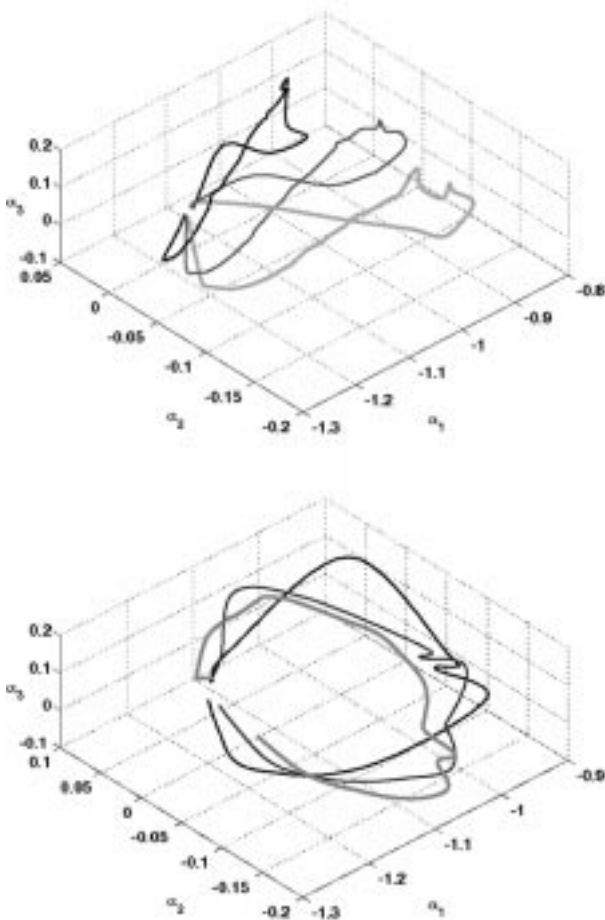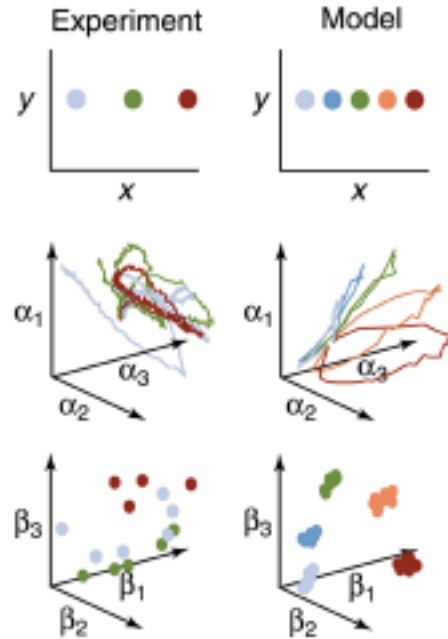

Fig. 8. (top) Phase trajectories in A-space corresponding to the responses to three stationary stimuli. (bottom) Equivalent picture for three moving stimuli.

and $\langle \cdot, \cdot \rangle$ stands for the standard inner product notation. The time coefficients of the KL expansion (2) are uncorrelated, i.e., no further compression (decorrelating) is possible. Furthermore, the average kinetic energy of the pth-order approximation of the movie k is given by

$$E_k = \frac{1}{m} \sum_{j=1}^{p} \sum_{i=1}^{m} [\alpha_j^k(i)]^2.$$

This result is straightforward and follows from the definition of the average kinetic energy, (2), and the fact that the principal modes are orthonormal. Thus, the fraction of the average kinetic energy of the kth movie captured by its pth-order approximation is given by

$$x_k = \frac{\sum_{j=1}^{p} \sum_{i=1}^{m} [\alpha_j^k(i)]^2}{\sum_{j=1}^{n^2} \sum_{i=1}^{m} [\alpha_j^k(i)]^2}.$$

It has been observed in the analysis that the first few principal components capture most of the energy content of a movie. In particular, $p = 3$ implies $x_k > 0.99$, indicating that the third-order approximation carries over 99% of the signal energy. Originally, movie frames are resampled to a 64×64 resolution ($n = 64$). However, the portions of the snapshots corresponding to out of range data have to be excluded from the analysis. Recall that these pixels were assigned NaN values, and as such could not be incorporated in the analysis. These pixels could be assigned some value other than NaN, but such an action would correlate the data additionally, and the high degree of compression would not be a genuine wave phenomenon, but a consequence of this action. Therefore, we take a squared subimage out of each snapshot and perform the analysis on

the subimages. The subimages are at 40×40 resolution and the area of the cortex that they cover is shown in Fig. 4. This area contains on average 350 pyramidal neurons out of 680. Three principal modes $M_1(x, y)$, $M_2(x, y)$, and $M_3(x, y)$ of the global basis of both stationary and moving data are shown in Fig. 7. These modes are found from (1) for $N = 1000$, $m = 201$, and $n = 40$. Therefore, the difference between two movies will be visible in their time coefficients $\alpha_1(t)$, $\alpha_2(t)$, and $\alpha_3(t)$. Said equivalently, the kth spatiotemporal signal $I^k(x, y, t)$ is represented by a phase trajectory in a 3-D space of time coefficients, and this space will be referred to as A-space. In Fig. 8, we show the phase portraits (plots of the time coefficients) corresponding to the responses to three stationary and three moving stimuli.

Because the positions of neurons in the model cortex are randomized with each new simulation, the vector function $[\alpha_1(t) \quad \alpha_2(t) \quad \alpha_3(t)]$ can be viewed as a random process. Statistical analysis of a random process can be facilitated if the process is further parameterized using a second KL decomposition. As outlined above, we form an average correlation matrix $C_2 \in \mathbb{R}^{3m \times 3m}$ as

$$C_2 = \frac{1}{N} \sum_{k=1}^{N} [\alpha_1^k(t) \quad \alpha_2^k(t) \quad \alpha_3^k(t)]^T$$
$$\times [\alpha_1^k(t) \quad \alpha_2^k(t) \quad \alpha_3^k(t)] \quad (3)$$

where

$$\alpha_i^k(t) = [\alpha_i^k(1), \alpha_i^k(2), \ldots, \alpha_i^k(m)] \qquad (i = 1, 2, 3).$$

The qth-order successive approximation of the kth random vector $[\alpha_1^k(t) \quad \alpha_2^k(t) \quad \alpha_3^k(t)]$ is given by

$$[\hat{\alpha}_1^k(t) \quad \hat{\alpha}_2^k(t) \quad \hat{\alpha}_3^k(t)] = \sum_{j=1}^{q} \beta_j^k \phi_j(t) \quad (4)$$

where $\phi_1(t), \ldots, \phi_q(t)$ are the eigenvectors corresponding to the largest q eigenvalues of the matrix C_2 written in the form $1 \times 3m$ rather than $3m \times 1$. The coefficients $\beta_j^k \in \mathbb{R}$ are found by orthogonal projection of a random process to the jth eigenvector

$$\beta_j^k = \langle [\alpha_1^k(t) \quad \alpha_2^k(t) \quad \alpha_3^k(t)], \phi_j(t) \rangle.$$

Combining results after the double data compression leads to a convenient representation of the kth spatiotemporal signal by a point in $\mathbb{R}^q$, i.e.,

$$I^k(x, y, t) \rightarrow [\beta_1^k, \beta_2^k, \ldots, \beta_q^k].$$

In our analysis, we use a third-order approximation ($q = 3$) and each data set is represented by a point in 3-D space, conveniently denoted B-space. Because of the randomness in the model, presentation of the same stimulus does not produce the same response in general. In particular, the same stimulus applied to several randomly generated cortical networks would produce as many points in B-space as the number of networks. These points appear clustered in B-space, and these clusters move in B-space as the parameters of the stimulus (e.g., position or velocity) change. The illustration of this phenomenon is shown in Fig. 9, where the model data is compared with the experimental

results. It should be noted that the points from experimental data are not as clustered as the model data. This could be a consequence of a considerable level of noise in the experiments.

IV. ESTIMATION WITH PRINCIPAL COMPONENTS ANALYSIS

In Section III, we have seen how the visual space can be mapped into a 3-D space of coefficients via the principal components representation of the associated spatiotemporal signal in the model cortex. The B-space construction has been detailed separately for the stationary and moving case. In this section, we show how a straightforward Bayesian detection algorithm can be used to estimate the position of an unknown spot of light or the velocity of an unknown moving spot of light in the visual space.

As discussed earlier, a set of 1000 simulations for both the stationary and moving cases is considered. Each of 1000 movies is represented by a point in B-space. The B-space plot of the points $[\beta_1, \beta_2, \beta_3]$ is shown in Fig. 10 for both stationary and moving case. The points in B-space elicited by the same stimulus appear clustered, with some of the clusters overlapping. This indicates that certain stimuli are perceived with ambiguity, e.g., *input 3*, *input 4*, and *input 5* in the stationary case and *input 10*, *input 11*, and *input 12* in the moving case (see Fig. 10). In the eventual process of detection, it would not be clear to which clusters these points belong. It seems that the vectors in B-space, even though 3-D, can be discriminated based on $[\beta_2, \beta_3]$ pairs only. Assuming the points within clusters are normally distributed, the conditional density function $f(\beta_2, \beta_3 | i_k)$ of point $[\beta_2, \beta_3]$ given input i_k can analytically be found as shown in Fig. 11. Given a response to an unknown stationary(moving) input i^*, the representation of the response is found as a vector $[\beta_1^*, \beta_2^*, \beta_3^*]$ in B-space. Using Bayes rule, the conditional probability density

$$f(i_k | \beta_2^*, \beta_3^*) = \frac{f(\beta_2^*, \beta_3^* | i_k) f(i_k)}{\sum_{j=1}^{20} f(\beta_2^*, \beta_3^* | i_j) f(i_j)} \quad (5)$$

can be calculated for every $k = 1, \ldots, 20$, and where the probability density function of the discrete random variable i_j is understood as a simple probability. The ML is then used to determine the most likely position (velocity) of the unknown input

$$\max_k f(i_k | \beta_2^*, \beta_3^*). \quad (6)$$

It is interesting to note that the condition $f(i_j | \beta_2, \beta_3) = f(i_k | \beta_2, \beta_3)$ for some $j, k = 1, \ldots, 20$ and $j \neq k$ defines a curve of constant likelihood ratio, and could be used to partition a decision space [24]. This might be useful for avoiding an explicit calculation every time a new estimation is to be performed, as the sample associated with an unknown parameter would fall in one of the existing ML bins. Assuming equal prior probabilities of each of the 20 inputs, the ML bin of the input i_k is simply given by

$$D_k = \{(\beta_2, \beta_3): f(\beta_2, \beta_3 | i_k) > f(\beta_2, \beta_3 | i_j), \quad \forall j \neq k\}.$$

The illustration of decision space for both stationary and moving stimuli is shown in Fig. 12. To test our estimation algorithm, we generated a set of 20 inputs for both stationary and moving cases. These inputs are the same as the ones used to construct
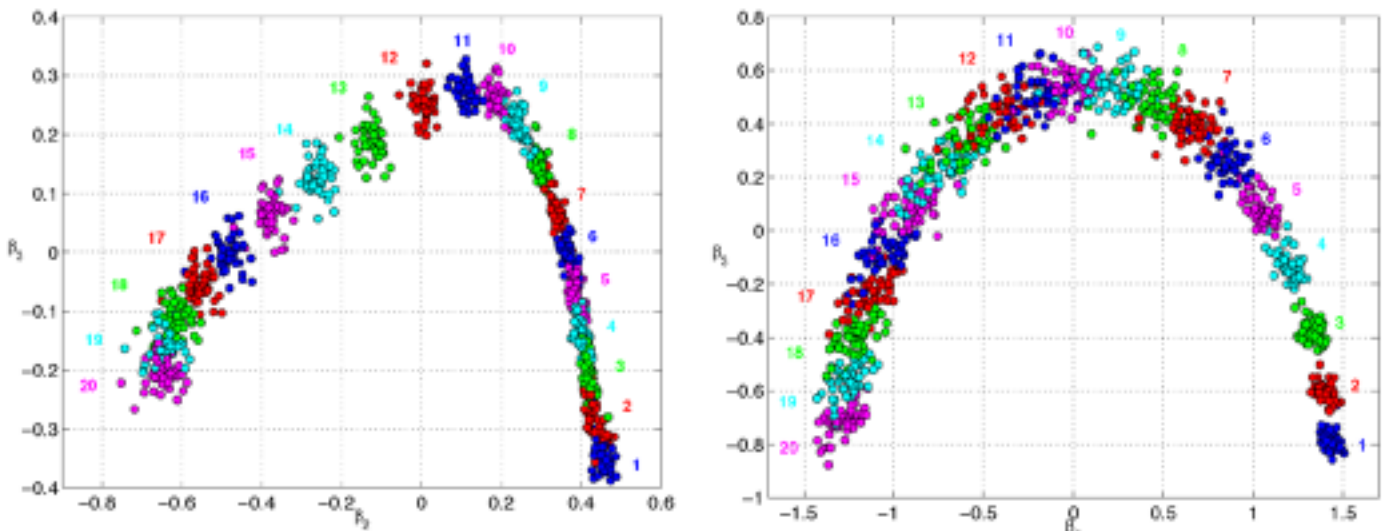
Fig. 10. Clusters of points in B-space corresponding to different (a) stationary stimuli and (b) moving stimuli. Each cluster contains 50 points as a result of applying the same stimulus to 50 different cortical samples. The numbers near the clusters indicate the label of the input responsible for those clusters. The 2-D versions of the plots are shown for clarity.
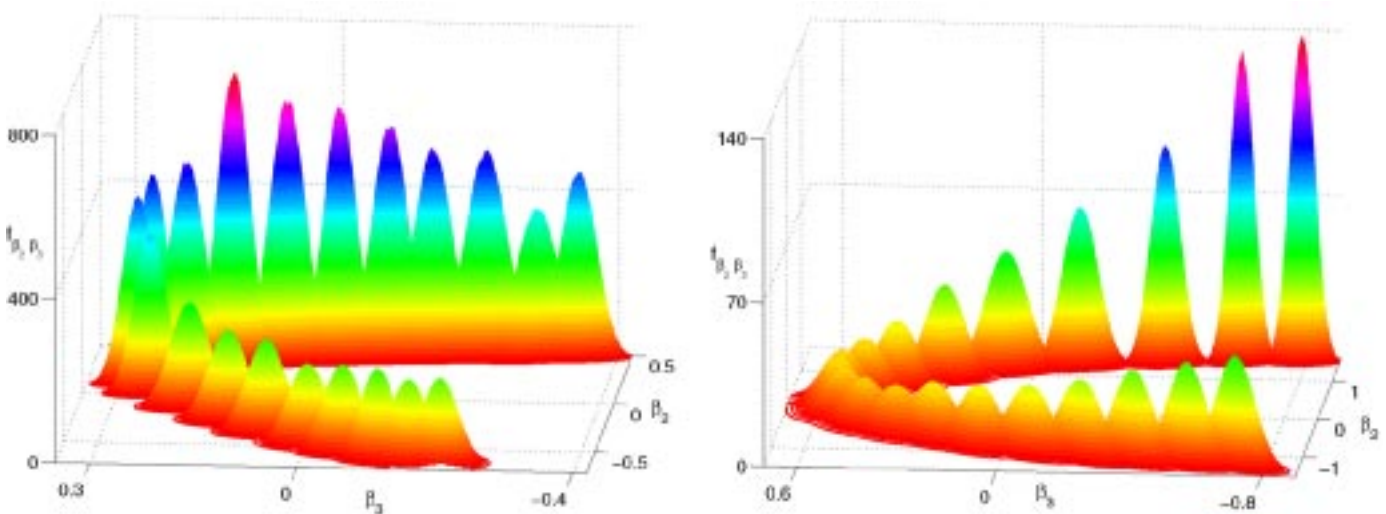

Fig. 11. (top) Conditional probability density functions given stationary stimuli. (bottom) Conditional probability density functions given moving stimuli.

Fig. 12. (a) Decision space corresponding to stationary stimuli. (b) Decision space corresponding to moving stimuli. The regions of different colors represent the bins of ML given a specific input. The numbers associated with each likelihood bin denote the label of the most likely input for that bin. Note that the likelihood bins for *input 9* and *input 10* are not connected in the stationary case. The bin colors are matching the colors of clusters in Fig. 10. White dots represent the observations obtained as a response to a set of 20 stimuli.

the conditional probability density functions, but they are applied to a randomly generated cortical network not belonging to the existing set of 50 networks used to build statistics (clusters). The corresponding waves have been recorded and decomposed using the procedure described in the previous sections. This results in a set of 20 points in B-space, where each point is presumably coming from one of the 20 clusters whose statistical descriptions have already been found. Depending on its position in the decision space, each point has been assigned to a particular likelihood bin, and these points are represented by the white dots in Fig. 12. It is evident from Fig. 12 that most of the points are found to belong to the bin corresponding to the input which indeed elicited the response. The results are somewhat better in the stationary case, as we found only two falsely detected parameters (see Fig. 12); *input 18* is found in bin 19 and input *input 19* is found in bin 20 together with the correctly detected *input 20*. In the moving case, we found several inputs that are falsely detected. An explicit calculation for falsely detected inputs has been performed using (5) and (6) and the results are summarized in Table I. For example, the response to *input 4* is found to most likely belong to bin 5, which is to say that *input 4* is falsely detected as *input 5* since there is a 0.7441 likelihood that such response is elicited by *input 5*. At this point we shall explain the source of errors in the estimation algorithm proposed. Clearly, the accuracy of estimation will be determined by the level of noise in the system. Recall that the network of the neurons obeys a certain density law only as a collection. That is, the exact positions of individual neurons are randomized within each rectangular block. Secondly, we have discretized our decision space into a set of 20 inputs, resulting in a set of 20 clusters which are frequently overlapping. Consequently, the Gaussian blobs within Fig. 11 are intersecting along the curves of relatively high likelihood, which may result in ambiguity during estimation and can lead to a false detection. Finally, the estimation method is based on 2-D conditional probability density functions, even though the vectors in the B-space are 3-D. The only reason we chose estimation in two dimensions is that the points were seemingly separable based on $[\beta_2, \beta_3]$ pairs only. This further led to a simple picture, the probability density functions could be visualized and the decision spaces were simple regions in a plane. It is expected that taking into account the third coordinate β_1 would improve the detection algorithm. The 3-D counterpart of (5) is given by

$$f(i_k|\beta_1^*, \beta_2^*, \beta_3^*) = \frac{f(\beta_1^*, \beta_2^*, \beta_3^*|i_k)\, f(i_k)}{\sum\limits_{j=1}^{20} f(\beta_1^*, \beta_2^*, \beta_3^*|i_j)\, f(i_j)} \quad (7)$$

and the most likely value of the unknown parameter is found by

$$\max_k f(i_k|\beta_1^*, \beta_2^*, \beta_3^*).$$

The MLs for the moving case based on 3-D algorithm are given in Table II. The likelihoods are shown only for the parameters that were falsely detected using 2-D algorithm (Table I). It is clear that the 3-D algorithm has a better performance, resulting in no falsely detected inputs. A similar result has been obtained for the stationary case.

TABLE I
LIKELIHOODS OF FALSELY DETECTED INPUTS CALCULATED FROM (5) FOR MOVING CASE ARE SHOWN BELOW. THE BOXED VALUES ARE THOSE OF ML FOR A GIVEN INPUT

Bin \ Input	4	5	6	7	11
4	0.2559	0.0000	0.0000	0.0000	0.0000
5	0.7441	0.0100	0.0000	0.0000	0.0000
6	0.0000	0.9852	0.0165	0.0000	0.0000
7	0.0000	0.0048	0.9688	0.1774	0.0000
8	0.0000	0.0000	0.0147	0.7896	0.0000
9	0.0000	0.0000	0.0000	0.0330	0.0000
10	0.0000	0.0000	0.0000	0.0000	0.0116
11	0.0000	0.0000	0.0000	0.0000	0.3524
12	0.0000	0.0000	0.0000	0.0000	0.5818
13	0.0000	0.0000	0.0000	0.0000	0.0539
14	0.0000	0.0000	0.0000	0.0000	0.0003

TABLE II
LIKELIHOODS OF PREVIOUSLY FALSELY DETECTED INPUTS CALCULATED FROM (7) FOR MOVING CASE. ALL INPUTS ARE CORRECTLY DETECTED AS INDICATED BY THE VALUES OF MLs

Bin \ Input	4	5	6	7	11
3	0.0000	0.0000	0.0000	0.0000	0.0000
4	1.0000	0.0000	0.0000	0.0000	0.0000
5	0.0000	0.9987	0.0000	0.0000	0.0000
6	0.0000	0.0013	0.9983	0.0000	0.0000
7	0.0000	0.0048	0.0017	1.0000	0.0000
8	0.0000	0.0000	0.0000	0.0000	0.0000
9	0.0000	0.0000	0.0000	0.0000	0.0000
10	0.0000	0.0000	0.0000	0.0000	0.0035
11	0.0000	0.0000	0.0000	0.0000	0.9942
12	0.0000	0.0000	0.0000	0.0000	0.0023

V. CONCLUSION

The main contribution of this paper is twofold. First, we were able to synthesize a large-scale model of the turtle visual cortex knowing the biophysical parameters of the individual cells and basic aspects of the geometry of interconnections between neurons. Without going into details of the modeling process, we give a comprehensive description of the model with a special emphasis on the properties of the actual visual cortex that are preserved in the model. Our model has shown the basic qualitative features of the turtle visual cortex such as the production of the cortical wave in response to stationary and moving stimuli. Similar qualitative behavior has been observed experimentally using voltage-sensitive dye techniques. Our second contribution is to demonstrate that the spatiotemporal dynamics of the cortical waves provide a means to map the visual space onto B-space that encodes the position and velocity parameters of a spot of light in the visual space. Assuming Gaussian conditional density functions and using ML estimate, we are able to detect the unknown parameters in the visual space.

As a final remark, the results in this paper require several comments. The first is that the current version of model includes only the visual cortex. Neurons in the dorsal LGN are included only as a series of one compartment models arranged along a line. They do not adequately represent the two-dimensional structure of the retinal projection to the dorsal lateral geniculate. Retinal ganglion cells in turtles have complex receptive

field properties that are not included in the model. It is not surprising, then, that the waves in our simulations are not as complex as those seen *in vivo* by Prechtl *et al.* [6]. Nonetheless, it is important to note that KL decomposition has been successfully applied to *in vivo* results by Senseman and Robbins [25], so it is likely that our approach to analyzing the information content of cortical waves can be applied to *in vivo* as well as *in vitro* results. Second, KL decomposition as presented in this paper uses the concept of global bases in space and time, obtained by spatial and temporal averaging, respectively. It may be possible that not all parts of the cortex have equal importance in the encoding process. Furthermore, the time response could have different relevance at different stages (transient vs. steady state). All of this information is lost in the process of averaging once the global bases are calculated. An important question is if all parts of the cortex are carrying information equally, as opposed to some parts carrying more information. The latter possibility would necessarily lead to a different choice of basis functions, perhaps ones that are localized in both space and time.

ACKNOWLEDGMENT

REFERENCES

[1] F. Delcomyn, *Foundations of Neurobiology*. New York: Freeman, 1998.

[2] P. Z. Mazurskaya, "Organization of receptive fields in the forebrain of *emys orbicularis*," *Neurosci. Behav. Physiol.*, vol. 7, pp. 311–318, 1974.

[3] D. M. Senseman, "Correspondence between visually evoked voltage-sensitive dye signals and activity recorded in cortical pyramidal cells with intracellular microelectrodes," *Vis. Neurosci.*, vol. 13, pp. 963–977, 1996.

[4] K. A. Robbins and D. M. Senseman, "Visualizing differences in movies of cortical activity," in *Proc. Visualization '98*, pp. 217–224, 536.

[5] ——, "Modal behavior of cortical neural networks during visual processing," *J. Neurosci.*, vol. 19, RC3, pp. 1–7, 1999.

[6] J. C. Prechtl, L. B. Cohen, P. P. Mitra, B. Pesaran, and D. Kleinfeld, "Visual stimuli induce waves of electrical activity in turtle visual cortex," *Proc. Nat. Acad. Sci. USA*, vol. 94, pp. 7621–7626, 1997.

[7] G. B. Ermentrout and D. Kleinfeld, "Traveling electrical waves in cortex: Insights from phase dynamics and speculation on computational role," *Neuron*, vol. 29, pp. 33–44, Jan. 2001.

[8] L. M. Smith, F. F. Ebner, and M. Colonier, "The thalamocortical projection in *pseudemys* turtles: A quantitative electron microscope study," *J. Comput. Neurol.*, vol. 190, pp. 445–461, 1980.

[9] K. A. Mulligan and P. S. Ulinski, "Organization of geniculocortical projections in turtles: Isoazimuth lamellae in the visual cortex," *J. Comput. Neurol.*, vol. 296, pp. 531–547, 1990.

[10] L. J. Larson-Prior, P. S. Ulinski, and N. T. Slater, "Excitatory amino acid receptory-mediated transmission in geniculocortical and intracortical pathways within visual cortex," *J. Neurophysiol.*, vol. 66, pp. 293–306, 1991.

[11] A. R. Kriegstein and B. W. Connors, "Cellular physiology of the turtle visual cortex: Synaptic properties and intrinsic circuitry," *J. Neurosci.*, vol. 6, pp. 178–191, 1986.

[12] Z. Nenadic, "Signal processing, computation and estimation in biological neural networks," Ph.D. dissertation, Washington Univ, St. Louis, MO, 2001.

[13] J. F. Colombe and P. Ulinski, "Temporal dispersion windows in cortical neurons," *J. Comput. Neurosci.*, vol. 7, pp. 71–87, 1999.

[14] J. G. Mancilla, M. Fowler, and P. Ulinski, "Responses of regular spiking and fast spiking cells in turtle visual cortex to light flashes," *Vis. Neurosci.*, vol. 15, pp. 979–993, 1998.

[15] J. G. Mancilla and P. Ulinski, "Role of gabaa-mediated inhibition in controlling the responses of regular spiking cells in turtle visual cortex," *Vis. Neurosci.*, vol. 18, pp. 9–24, 2001.

[16] C. E. Cosans and P. Ulinski, "Spatial organization of axons in turtle visual cortex: Intralamellar and interlamellar projections," *J. Comput. Neurol.*, vol. 296, pp. 548–558, 1990.

[17] J. M. Bower and D. Beeman, *The Book of Genesis*. Santa Clara, CA: TELOS, 1998.

[18] Z. Nenadic, B. K. Ghosh, and P. S. Ulinski, "Propagating waves in visual cortex: A large-scale model of turtle visual cortex," *Int. J. Math. Comput. Modeling*, 2002, to be published.

[19] P. A. Salin and D. A. Prince, "Electrophysiological mapping of gabaa receptor mediated inhibition in adult rat somatosensory cortex," *J. Neurophysiol.*, vol. 75, pp. 293–306, 1991.

[20] D. M. Senseman, "Spatiotemporal structure of depolarization spread in cortical pyramidal cell populations evoked by diffuse retinal light flashes," *Vis. Neurosci.*, vol. 16, pp. 65–79, 1999.

[21] P. Holmes, J. L. Lumley, and G. Berkooz, *Turbulence, Coherent Structure, Dynamical Systems and Symmetry*. Cambridge, U.K.: Cambridge Univ. Press, 1996.

[22] K. R. Rao and P. C. Yip, *The Transform and Data Compression Handbook*. Boca Raton, FL: CRC, 2001.

[23] M. Dellnitz, M. Golubitsky, and M. Nicol, "Symmetry of attractors and the Karhunen–Loeve decomposition," in *Trends and Perspectives in Applied Mathematics*, L. Sirovich, Ed. New York: Springer-Verlag, 1994, ch. 4, pp. 73–108.

[24] H. L. Van Trees, *Detection, Estimation and Modulation Theory*. New York: Wiley, 1968.

[25] D. M. Senseman and K. A. Robbins, "High speed vsd imaging of visually evoked cortical waves: Decomposition into intra- and intercortical wave motions," *J. Neurophysiol.*, 2002, to be published.

Zoran Nenadic received the B.S. degree in control engineering from the University of Belgrade, Belgrade, Yugoslavia, in 1995 and the M.S. and D.Sc. degrees in systems science and mathematics from Washington University, St. Louis, MO, in 1998 and 2001, respectively.

He is currently a Postdoctoral Fellow with the Division of Engineering and Applied Science, the California Institute of Technology, Pasadena, CA. His research interests are in the area of computational neuroscience, signal processing, and applications of control theory in biological systems.

Bijoy K. Ghosh (S'78–M'79–SM'90–F'00) received the B.Tech. and M.Tech. degrees in electrical and electronics engineering from BITS, Pilani, and the Indian Institute of Technology, Kanpur, India, and the Ph.D. degree in engineering from the Decision and Control Group of the Division of Applied Sciences, Harvard University, Cambridge, MA, in 1977, 1979, and 1983, respectively.

Since 1983, he has been a Faculty Member in the Systems Science and Mathematics Department, Washington University, St. Louis, MO, where he is currently a Professor and directs the center for BioCybernetics and Intelligent Systems. His research interests are in multivariable control theory, machine vision, robotic manufacturing, and biosystems and control.

Philip S. Ulinski received the Ph.D. degree in zoology from Michigan State University, East Lansing, in 1968.

He is currently Professor and Chairman of the Committee on Computational Neuroscience at the University of Chicago, Chicago, IL. His research interests include the functional organization of the cerebral cortex and computational models of neural circuits.